

## Microwave inverse Čerenkov accelerator

T. B. Zhang,<sup>1,2</sup> T. C. Marshall,<sup>1,2</sup> M. A. LaPointe,<sup>1</sup> J. L. Hirshfield,<sup>1,3</sup> and Amiram Ron<sup>1,4</sup>

<sup>1</sup>*Omega-P, Inc., 202008 Yale Station, New Haven, Connecticut 06520*

<sup>2</sup>*Department of Applied Physics, Columbia University, New York, New York 10027*

<sup>3</sup>*Physics Department, Yale University, New Haven, Connecticut 06520-8120*

<sup>4</sup>*Department of Physics, Technion-Israel Institute of Technology, Haifa 3200, Israel*

(Received 22 March 1996)

Analysis and experimental tests have been carried out on a dielectrically lined waveguide, which appears to be a suitable structure for accelerating electrons. From the dispersion relation for the  $TM_{01}$  mode, inner and outer radii of a copper-clad alumina pipe ( $\epsilon = 9.40$ ) have been determined such that the phase and group velocities are  $0.9732c$  and  $0.1096c$ , respectively. Analysis and particle simulation studies for the injection of 6-MeV microbunches from a 2.856-GHz rf gun, and subsequent acceleration by the  $TM_{01}$  fields, predict that an acceleration gradient of 6.3 MV/m can be achieved with a traveling-wave power of 15 MW applied to the structure. Synchronous injection into a narrow phase window is shown to allow trapping of all injected particles. The rf fields of the accelerating structure are shown to provide radial focusing, so that longitudinal and transverse emittance growth during acceleration is small and that no external magnetic fields are required for focusing. The acceleration mechanism is the inverse of that in which electrons radiate as they traverse a waveguide at speeds exceeding the phase velocity of the microwaves (Čerenkov radiation) and is thus referred to as a microwave inverse Čerenkov accelerator. For 0.16-nC, 5-psec microbunches, the normalized emittance of the accelerated beam is predicted to be less than  $5\pi$  mm mrad. Experiments on sample alumina tubes have been conducted that verify the theoretical dispersion relation for the  $TM_{01}$  mode over a two-to-one range in frequency. No excitation of axisymmetric or nonaxisymmetric competing waveguide modes was observed. High power tests showed that tangential electric fields at the inner surface of an uncoated sample of alumina pipe could be sustained up to 8.4 MV/m without breakdown. These considerations suggest that a microwave inverse Čerenkov test accelerator can be built to examine these predictions using an available rf power source, a 6-MeV rf gun, and an associated beam line. [S1063-651X(96)07408-9]

PACS number(s): 41.60.Cr, 41.75.Ht, 29.17.+w

### I. INTRODUCTION

The stimulated Čerenkov effect is a well-understood mechanism for generating coherent radiation from an energetic electron beam [1–3]. The radiating electrons move at speed greater than that of the velocity of light in the structure (hence the name Čerenkov); although there are several ways to slow light waves, as a general rule the term is used when the slowing is caused by a dielectric element. When one does a linearized treatment of the fields and the self-consistent motion of the particles, a dispersion relation is obtained for growth or decay of radiation in the system. One of the three roots obtained corresponds to a damped wave; this we identify with the mechanism of stimulated absorption, whereby an electron will gain energy at the expense of the rf field. In the discussion that follows we consider the application of stimulated absorption in the nonlinear regime of particle trapping, which applies to an electron accelerator device. This we refer to as a microwave inverse Čerenkov accelerator (MICA) [4].

Acceleration of the electron is done by appropriate phasing of a 6-MeV electron bunch that is emitted from a thermionic cathode rf gun, so that a continuous accelerating force is applied to all the electrons, which move synchronously with the slow rf wave. Variation of the wave speed, if necessary, can be done by using a small taper in the filling factor of the dielectric element. Thus the device resembles a rf linear accelerator but without the periodic loading structures

in the waveguide. As the MICA is a smooth bore and the motion of the particles is rather one dimensional, we expect that the quality of the electron beam produced will be attractive. The MICA under consideration will use a SLAC (Stanford Linear Accelerator) source of microwave power at 2.856 GHz, and with a bunch length of only 5 psec compared to the rf period of 350 psec, we can expect excellent trapping and acceleration of a monoenergetic bunch of electrons. Another approach [5–8], the inverse Čerenkov accelerator experiment at Brookhaven National Laboratory, uses a  $CO_2$  laser and an axicon to accelerate an electron beam at 40 MeV energy; the light wave is slowed by introducing hydrogen gas into the beam line. The gas contributes to some electron scattering, and the main disadvantage of the short laser wavelength is that electrons interact with the wave over the full range ( $2\pi$ ) of phase; that is, the bunch length is long compared to the rf wavelength. In the MICA, the electrons move down a 1-cm-diam hole in an alumina dielectric liner as a filamentary beam of under 1 mm diameter. The main limitation here is that of the maximum axial field gradient (120–160 kV/cm [9]) along the dielectric surface. Shown in Fig. 1 is a schematic layout of the MICA.

In this paper we describe first the analysis of a wave inside a dielectric annular cylinder fitted into a cylindrical waveguide. We find dispersion relations [10] for the axisymmetric  $TM_{0n}$ -like mode of the system, that is, the mode that gives a maximum electric field along the axis. This calculation provides both the slowing factor and the distribution of

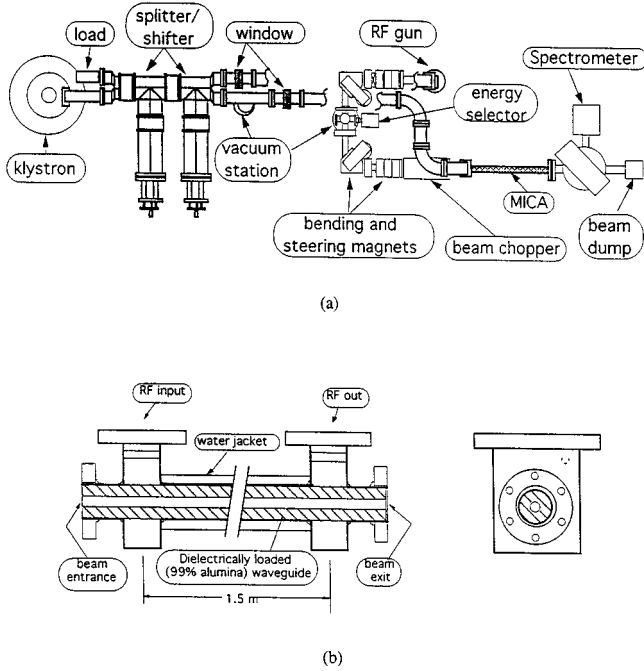


FIG. 1. (a) Schematic diagram of the MICA layout. A preaccelerated short bunch of  $\sim 6$ -MeV electrons from a rf gun is injected in the appropriate accelerating phase into the MICA, so that trapping and further acceleration of the entire bunch can occur. (b) MICA accelerating section.

fields. In Sec. III we analyze the power flow and energy attenuation of the rf field in the loaded waveguide and find the group velocity of the field. Based on the single-particle dynamics, we then, in Sec. IV, model the acceleration and motion of electrons in the vacuum fields of this device. We will show that the beam off-axis effect is not important in the MICA. We anticipate that the electron beam self-field effect is negligible and the normalized emittance is constant throughout the acceleration of the bunch, and this is established by making use of the detailed accelerator code PARMELA in Sec. V. Knowledge of the rf breakdown limits of the dielectric relates to the maximum acceleration gradient of the beam, and therefore we design and construct a cavity resonator with an alumina liner for the breakdown limit test, which is described in Sec. VI. We conclude with a summary in Sec. VII. The objective of this effort is to determine whether a compact high-quality accelerator of this type is feasible, and we find that the answer is positive.

## II. DISPERSION RELATION AND FIELD DISTRIBUTION OF THE DIELECTRIC-LOADED WAVEGUIDE

The MICA configuration is a circular waveguide loaded by high- $\epsilon$  dielectric material, with a small hole on axis for passage of the beam as shown in Fig. 2. Before selecting this configuration we explored another dielectric structure, a rectangular waveguide loaded by a dielectric slab or slabs. No conventional TM or TE modes exist in the latter, but rather longitudinal-section electric modes or longitudinal-section magnetic modes with either zero electric or zero magnetic field normal to the dielectric surface [11]. The maximum

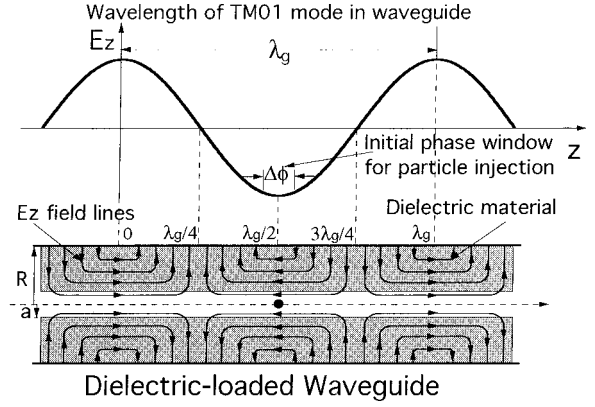


FIG. 2. Longitudinal cross section of the loaded waveguide showing the axial electric field distribution as well as electron phase positions along the waveguide.

axial field strength occurs inside the vacuum-dielectric interface and so this configuration is not appropriate for electron acceleration. However, the use of a high- $\epsilon$  annulus inside a circular waveguide maintained a large uniform  $E_z$  field inside the hole, which is ideal for an accelerator.

### A. Dispersion relation and eigenmodes

The axisymmetric modes of this cylindrical dielectric-loaded system are either TE or TM, and we consider the  $TM_{0n}$ -like mode of this system, i.e., the mode with finite axial electric field on axis, no azimuthal variations, and one radial maximum for the axial electric field. Using the appropriate boundary conditions at the interface of two differing media as well as at the outer metallic conducting wall, we solve the Maxwell equations using standard procedures [10] and arrive at a dispersion relation of the system for  $TM_{0n}$  eigenmodes, namely,

$$\frac{I_1(k_{1i}a)}{I_0(k_{1i}a)} = \frac{\epsilon_2 k_{1i} J_1(k_{\perp 2}a) N_0(k_{\perp 2}R) - J_0(k_{\perp 2}R) N_1(k_{\perp 2}a)}{\epsilon_1 k_{\perp 2} J_0(k_{\perp 2}a) N_0(k_{\perp 2}R) - J_0(k_{\perp 2}R) N_0(k_{\perp 2}a)}, \quad (2.1)$$

where the functions of  $J_m(x)$  and  $N_m(x)$  are  $m$ th-order Bessel functions of the first and second kinds and  $I_m(x)$  is the modified Bessel function;  $a$  and  $R$  are radii of the central vacuum hole and the outer waveguide wall, respectively, and  $\epsilon_1$  and  $\epsilon_2$  are the dielectric constants of the inner and outer regions. Obviously, for the central vacuum hole  $\epsilon_1 = 1$ . Note the  $k_{\perp 1}$  and  $k_{\perp 2}$  are the transverse wave numbers in region 1 and 2, and in Eq. (2.1), we have substituted  $k_{1i}^2 = -k_{\perp 1}^2$  for the slow wave, so that

$$k_{1i}^2 = k_z^2 - \epsilon_1 k_0^2, \quad (2.2)$$

$$k_{\perp 2}^2 = \epsilon_2 k_0^2 - k_z^2, \quad (2.3)$$

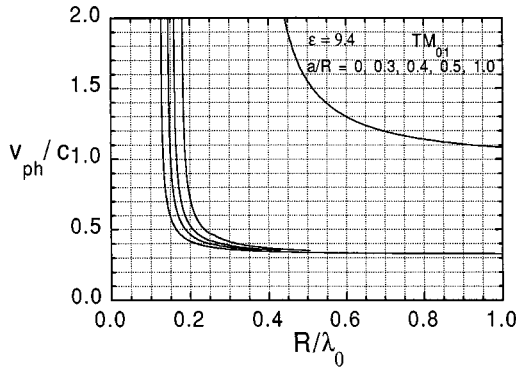


FIG. 3. Normalized phase velocity  $v_{ph}/c$  vs normalized outer radius  $R/\lambda_0$  for the  $TM_{01}$  mode waveguide with an alumina liner when the radius of the vacuum hole varies. From left to right,  $a/R=0$  (completely filled), 0.3, 0.4, 0.5, and 1.0 (vacuum waveguide). Note that for  $a/R=0.3$ ,  $v_{ph} \leq c$  for  $R \geq 0.15\lambda_0$ .

where  $k_z$  is the axial wave number of the waveguide  $TM_{0n}$  mode and  $k_0 = \omega/c$  is the wave number in free space for a wave of radian frequency  $\omega$ . Combining Eqs. (2.2) and (2.3), we have

$$k_{\perp 2}^2 = (\varepsilon_2 - \varepsilon_1)k_0^2 - k_{1i}^2. \quad (2.4)$$

By eliminating  $k_{\perp 2}$  from Eq. (2.1) using Eq. (2.4), we can solve for the multiple eigenvalues  $k_{1i}$  for the loaded waveguide, corresponding to distinct numbers  $n$  of radial maxima in the rf electric fields of the  $TM_{0n}$  modes. Accordingly, the normalized phase velocity  $v_{ph}$  and guide wavelength  $\lambda_g$  of each mode can be obtained from the respective eigenvalue. It then follows that

$$\frac{v_{ph}}{c} = \frac{\lambda_g}{\lambda_0} = \left(1 + \frac{k_{1i}^2}{k_0^2}\right)^{-1/2}, \quad (2.5)$$

where  $\lambda_0$  is the free space wavelength of the field. As an example, Fig. 3 shows the normalized phase velocity of the  $TM_{01}$  mode as a function of the ratio  $R/\lambda_0$ . For this example, the dielectric constant  $\varepsilon_2$  is taken to be 9.4 and the ratio of hole radius to outer dielectric radius  $a/R$  is taken to be 0 (completely filled), 0.3, 0.4, 0.5, and 1.0 (no dielectric at all). For the specific configuration of  $a/R=0.3$ , one finds from Fig. 3 (second curve from the left) that a phase velocity of  $c$  and below obtain when  $R/\lambda_0 > 0.15$ , from which one finds the design values of outer waveguide radius and hole radius in terms of the rf vacuum wavelength for a given desired phase velocity.

For operation at 2.856 GHz, the frequency of the rf source available for the MICA, one has  $\lambda_0 = 10.504$  cm. Since the injected 6-MeV electrons have velocities of about  $0.997c$ , the desired phase velocity is very close to  $c$ . From the curve in Fig. 3 with  $a/R=0.30$ , one selects  $R=1.59$  cm and  $a=0.48$  cm for  $v_{ph}/c \approx 1.0$ . The cutoff frequency of the  $TM_{01}$  mode is 2.69 GHz, and for the  $TM_{02}$  mode it is 6.72 GHz. By neglecting the hole, one can estimate cutoff frequencies for the  $TE_{11}$ -like and  $TE_{01}$  modes to be 1.80 and 3.76 GHz, respectively. The dimensions selected for operation at 2.856 GHz thus appear to guarantee freedom from

interference by other nearby modes, since only the  $TE_{11}$ -mode with nearly orthogonal polarization is not cut off at 2.856 GHz.

### B. rf field distributions

The electromagnetic fields that are distributed in the two regions are joined at the interior boundary between vacuum and the dielectric and satisfy conditions appropriate for a conducting metallic wall at the outer boundary. For the  $TM_{0n}$  modes, only three components exist (in cylindrical coordinates  $r, \theta, z$ ), namely,  $E_z$ ,  $E_r$ , and  $B_\theta$ . They have the following forms. When  $0 < r < a$  (region 1), one has

$$E_{z1}(r, z, t) = E_0 I_0(k_{1i}r) \cos(\omega t - k_z z), \quad (2.6)$$

$$E_{r1}(r, z, t) = -E_0 \frac{k_z}{k_{1i}} I_1(k_{1i}r) \sin(\omega t - k_z z), \quad (2.7)$$

$$B_{\theta 1}(r, z, t) = -E_0 \frac{\varepsilon_1 k_0}{k_{1i}} I_1(k_{1i}r) \sin(\omega t - k_z z). \quad (2.8)$$

When  $a < r \leq R$  (region 2), one has

$$E_{z2}(r, z, t) = E_0 G_0(k_{\perp 2}r) \cos(\omega t - k_z z), \quad (2.9)$$

$$E_{r2}(r, z, t) = -E_0 \frac{k_z}{k_{\perp 2}} G_1(k_{\perp 2}r) \sin(\omega t - k_z z), \quad (2.10)$$

$$B_{\theta 2}(r, z, t) = -E_0 \frac{\varepsilon_2 k_0}{k_{\perp 2}} G_1(k_{\perp 2}r) \sin(\omega t - k_z z), \quad (2.11)$$

where

$$g_i = \frac{I_0(k_{1i}a)}{J_0(k_{\perp 2}a)N_0(k_{\perp 2}R) - J_0(k_{\perp 2}R)N_0(k_{\perp 2}a)}, \quad (2.12)$$

$$G_0(k_{\perp 2}r) = g_i [J_0(k_{\perp 2}r)N_0(k_{\perp 2}R) - J_0(k_{\perp 2}R)N_0(k_{\perp 2}r)], \quad (2.13)$$

$$G_1(k_{\perp 2}r) = g_i [J_1(k_{\perp 2}r)N_0(k_{\perp 2}R) - J_0(k_{\perp 2}R)N_1(k_{\perp 2}r)]. \quad (2.14)$$

The amplitude  $E_0$  is the peak axial field strength on axis. Its value in the absence of a beam and with negligible power losses in the dielectric and the walls can be determined from the total microwave power transmitted through the waveguide after integrating the Poynting vector over the guide cross section. Figure 4 is a snapshot of relative amplitudes of the field components vs radial coordinates  $r/R$ . This is a field profile seen by a specific electron whose relative phase with respect to the field is very close to  $\pi$  and therefore it is accelerated by the maximum axial field while suffering little influence from the transverse field components. This result thus establishes that is indeed possible to design a dielectrically loaded waveguide where the axial electric field in the beam hole is nearly uniform with radius, having its strongest magnitude on axis, where the beam is to be located.

As the acceleration of electrons proceeds, the microwave field will gradually lose part of its energy to the electrons and therefore  $E_0$  will be a decreasing function of axial distance. However, the rf energy stored in the accelerating structure will be much larger than the energy to be imparted to the

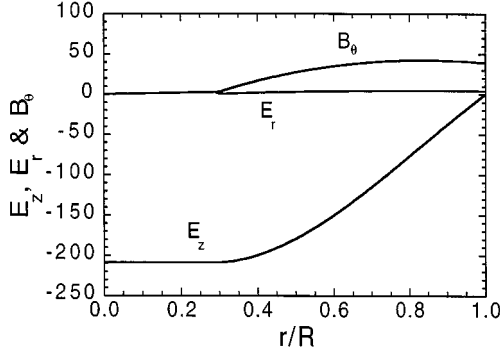


FIG. 4. Profile of field component amplitudes vs  $r/R$  for the  $TM_{01}$  mode with an alumina liner  $a/R=0.3$ . This is the field “seen” by an electron whose relative phase to the field is close to  $\pi$ ; the electron experiences an intense and uniform axial field but much smaller transverse fields.

microbunches that pass through in one fill time. As a result, rf power depletion along the MICA will be small, and it is a good approximation to neglect the small axial decrease of  $E_0$  along the beam path. Were the MICA to be operated with strong rf power depletion successive microbunches could encounter diminishing accelerating fields, the final energy of late-arriving microbunches could be significantly lower than that of early microbunches, and the overall beam energy spread could be substantial; this would defeat one goal of the research, namely, low-energy spread. A rf beam chopper would allow only one in ten (or even fewer) high-current microbunches to enter the MICA, thus ensuring negligible energy spread due to beam loading

### III. RF POWER FLOW, ENERGY DENSITY, AND ENERGY LOSS

The flow of energy in the loaded waveguide is described by the complex Poynting vector

$$\mathbf{S} = \frac{c}{4\pi} \frac{1}{2} (\mathbf{E} \times \mathbf{H}^*). \quad (3.1)$$

Accordingly, the energy density is

$$w = \frac{1}{8\pi} \frac{1}{2} (\mathbf{E} \cdot \mathbf{D}^* + \mathbf{B} \cdot \mathbf{H}^*). \quad (3.2)$$

Substituting Eqs. (2.6)–(2.11) in (3.1) and (3.2), we can represent  $\mathbf{S}$  and  $w$  in terms of the axial electric field in both regions. To evaluate the total power  $P$  and the field energy per unit length  $U$  of the waveguide, we integrate the axial component of  $\mathbf{S}$  and  $w$  over the cross-sectional areas, i.e.,  $P = \int \mathbf{S} \cdot d\mathbf{A}$  and  $U = \int w dA$ . The integration requires the use of Green’s first identity

$$\int_A |\nabla_{\perp} E_z|^2 dA = \oint c E_z^* \frac{\partial E_z}{\partial n} dl - \int_A E_z^* \nabla_{\perp}^2 E_z dA$$

on the boundary surfaces of each region [12]. The first integral vanishes on the outer surface of region 2 (perfect conductor condition). However, on the interface between the two regions, care must be taken to consider

TABLE I. Phase velocity and group velocity of the  $TM_{01}$  mode in the dielectric-loaded waveguide for different  $\epsilon_r$ .

| $\epsilon_r$ | $v_{ph}/c$ | $v_g/c$ |
|--------------|------------|---------|
| 9.35         | 0.9964     | 0.1076  |
| 9.40         | 0.9732     | 0.1096  |
| 9.45         | 0.9516     | 0.1115  |
| 9.50         | 0.9314     | 0.1133  |
| 9.55         | 0.9123     | 0.1150  |
| 9.60         | 0.8944     | 0.1168  |

$$\frac{\partial E_{z1}}{\partial n_1} = \nabla E_{z1} \cdot \mathbf{n}_1 = \frac{\partial E_{z1}}{\partial r}, \quad \frac{\partial E_{z2}}{\partial n_2} = \nabla E_{z2} \cdot \mathbf{n}_2 = -\frac{\partial E_{z2}}{\partial r},$$

where  $\mathbf{n}_1$  and  $\mathbf{n}_2$  are the unit normal vectors of regions 1 and 2 on the interface, respectively. By means of the eigenmode equations, the second integral may be reduced to the normalization integral for  $E_z$ ; then we have

$$\int_{A1} |\nabla_{\perp} E_{z1}|^2 dA = 2\pi a \left[ E_{z1}^* \frac{\partial E_{z1}}{\partial r} \right]_{r=a} + k_{\perp 1}^2 \int_{A1} |E_{z1}|^2 dA, \quad (3.3)$$

$$\int_{A2} |\nabla_{\perp} E_{z2}|^2 dA = -2\pi a \left[ E_{z2}^* \frac{\partial E_{z2}}{\partial r} \right]_{r=a} + k_{\perp 2}^2 \int_{A2} |E_{z2}|^2 dA. \quad (3.4)$$

Substituting Eqs. (3.3) and (3.4) into our integrations, consequently, we get the expressions for transmitted power and energy per unit length

$$P = \frac{\omega k_z}{8\pi} \left\{ \frac{\epsilon_1}{k_{\perp 1}^2} \int_{A1} |E_{z1}|^2 dA + \frac{\epsilon_2}{k_{\perp 2}^2} \int_{A2} |E_{z2}|^2 dA + 2\pi a \left[ E_{z1}^* \frac{\partial E_{z1}}{\partial r} \right]_{r=a} \frac{\epsilon_1}{k_{\perp 1}^2} \left[ \frac{1}{k_{\perp 1}^2} - \frac{1}{k_{\perp 2}^2} \right] \right\}, \quad (3.5)$$

$$U = \frac{k_0^2}{8\pi} \left\{ \frac{\epsilon_1^2}{k_{\perp 1}^2} \int_{A1} |E_{z1}|^2 dA + \frac{\epsilon_2^2}{k_{\perp 2}^2} \int_{A2} |E_{z2}|^2 dA + 2\pi a \left[ E_{z1}^* \frac{\partial E_{z1}}{\partial r} \right]_{r=a} \frac{\epsilon_1}{k_{\perp 1}^2} \left[ \frac{\epsilon_1}{k_{\perp 1}^2} - \frac{\epsilon_2}{k_{\perp 2}^2} \right] \right\}. \quad (3.6)$$

The last terms on the right-hand side of the above equations indicate power flow and energy in a surface wave that can exist only on the interface between two differing regions. Given the level of input rf power  $P$ , Eq. (3.5) can be used to determine the amplitude of the axial electric field  $E_0$ .

A comparison of the energy per unit length  $U$  with the power flow  $P$  shows that  $P$  and  $U$  are exactly proportional to one another. The constant of proportionality has the dimensions of velocity (velocity of energy flow) and can be identified with the group velocity  $v_g = P/U$ . Values of  $v_g/c$  and  $v_{ph}/c$  have been computed for the  $TM_{01}$ -mode MICA structure with  $a/R=0.30$  and  $R/\lambda_0=0.15$  for a variety of values of  $\epsilon_2$  ranging from 9.35 to 9.60, representing the spread cited for commercially produced alumina, depending upon purity. Results are listed in Table I. It is seen that the group velocity

of the  $TM_{01}$  mode in the loaded waveguide is much slower than the phase velocity. Checking these results, one may find they are very close to the relation  $v_{ph}v_g = c^2/\epsilon$ , the result for completely filled waveguide. The close agreement arises since the unfilled volume only occupies about 9% of the waveguide and the stored energy per unit length there is calculated to be only about 3% of the total.

MICA operation with  $v_g/c \approx 0.10$  would be similar to that of conventional rf linear accelerator operation, where low group velocities are also employed. In the MICA case, the bulk of the energy is stored in the high-dielectric-constant material, while in the conventional linear accelerator the bulk of the energy is stored in periodic structures that act similarly to cavities. Low group velocity implies that the energy fill-time is much longer than the microbunch transit time along an accelerator section, so that significant energy depletion would cause late-following bunches to experience less acceleration than early-leading bunches. After several fill times, a steady state can be reached, but beam loading will reduce the field amplitudes, bringing about less net acceleration than in the absence of beam loading. This situation is undesirable when the accelerator is designed for high-energy gain and high-energy resolution. Therefore one must ensure that the energy carried away by the beam during a sequence of microbunches (i.e., during one fill time  $\tau = L/v_g$ ) is much less than the stored energy. The available rf power is about 15 MW. For a group velocity  $v_g/c \approx 0.10$  and a length  $L = 150$  cm, the total stored rf energy  $UL = 0.75$  J and the fill time is 50 nsec. The estimated energy gain is 10 MeV. If one is to accelerate  $10^9$  electrons per microbunch (0.16 nC) then the energy gain per microbunch is 1.6 mJ, much smaller than the total stored energy. However, if one microbunch is injected into each rf cycle (i.e., each 350 psec), the number of microbunches per fill time is 143 and the energy carried away by the beam in one fill time would be 0.23 J, neglecting beam loading. Since this value is not negligible compared to the total stored energy of 0.75 J, significant beam loading would be expected and the estimate for energy gain is too large. This undesirable situation can be avoided in the MICA by use of a beam chopper that will reduce the number of microbunches per fill time by a factor of 10; details of the proposed beam chopper will be discussed elsewhere. It should be noted that beam loading as described here is independent of the particular accelerator structure and depends only upon the group velocity and fill time; usually low group velocity is chosen in linear accelerators to afford a higher acceleration gradient for the same available rf power, as compared with high group velocity.

Power flow considerations discussed so far have applied to waveguides with perfectly conducting walls and ideal lossless dielectric. The axial wave number  $kz$  above cutoff is purely real in that situation. However, in reality, the waveguide walls will have finite conductivity and the dielectric permittivity of the alumina medium will be complex. Both factors contribute to circuit dissipation, which might influence MICA operation. The above analysis has been extended to include both Ohmic wall losses and complex dielectric permittivity. We here summarize the results of these effects.

To consider the finite conductivity wall we employ the Poynting vector (3.1) to find the power dissipated in Ohmic losses per unit length of the guide, viz.,

$$\frac{dP_w}{dz} = \frac{c^2}{32\pi^2\sigma\delta} \oint_C \frac{\epsilon^2 k_0^2}{k_{\perp}^4} \left| \frac{\partial E_z}{\partial n} \right|^2 dl, \quad (3.7)$$

where the integral is taken around the boundary of the waveguide,  $\delta = (c/\sqrt{4\pi})(2/\mu_c\omega\sigma)^{1/2}$  is the skin depth, and  $\sigma$  is the electrical conductivity of the conductor. The above equation will allow us to calculate approximately the resistive losses for the dielectric-loaded waveguide and cavity, using the fields we have found for the idealized problem of infinite conductivity in Sec. II. For pure copper walls,  $\delta = 1.22 \times 10^{-4}$  cm at 2.856 GHz, one finds the attenuation along the MICA due to Ohmic wall losses to be 0.465 dB over its 150 cm length.

Turning to the dielectric losses, we express the complex dielectric constant as  $\epsilon_2 = \epsilon_r - i\epsilon_i$ . According to Eq. (2.3), we have

$$k_z^2 = k_{z0}^2 - i\epsilon_i k_0^2, \quad (3.8)$$

where  $k_{z0}^2 = \epsilon_r k_0^2 - k_{\perp 2}^2$  and  $k_{z0}$  is the value of the axial wave number for the perfect dielectric. We express the axial wave number for the dielectric as  $k_z = k_{zr} - ik_{zi}$ , and from Eq. (3.8), we solve approximately

$$k_{zr} \cong k_{z0} + \frac{1}{8} \epsilon_1^2 k_0 \left( \frac{k_0}{k_{z0}} \right)^3, \quad (3.9)$$

$$k_{zi} \cong \frac{1}{2} \epsilon_i k_0 \left( \frac{k_0}{k_{z0}} \right). \quad (3.10)$$

For alumina with  $\epsilon_r = 9.4$  and (typically)  $\epsilon_i/\epsilon_r = 9.4 \times 10^{-5}$ ,  $k_0 = 0.598$  (for  $f = 2.856$  GHz), and  $k_0/k_{z0} \approx 1$ , we get  $k_{zi} \approx 2.64 \times 10^{-4}$ . In the total length of the waveguide  $z = 150$  cm, the field amplitude will drop from unity to  $\exp(-k_{zi}z) \approx 0.96$  due to the dielectric losses, corresponding to an attenuation of 0.355 dB. The total attenuation due to dielectric and wall losses is 0.82 dB, corresponding to a diminution in field strength along the 150-cm accelerating section of 9.0%. The actual diminution might be expected to exceed this value, since the copper skin on the alumina pipe could have a conductivity lower than the ideal value. Furthermore, poor-quality alumina, with a loss tangent greater than  $10^{-4}$ , could also give rise to higher losses. These losses in both the copper skin and the dielectric will reduce the acceleration energy below that calculated for zero loss. This phenomenon is examined further in the following section.

#### IV. PARTICLE MOTION AND ACCELERATION IN THE WAVEGUIDE FIELDS

Substituting Eqs. (2.6)–(2.11) in the Lorentz force equation gives the change in relativistic momentum  $\mathbf{P} = m\gamma\mathbf{v}$  of the beam particles in the MICA, namely,

$$\frac{d\mathbf{P}}{dt} = -e \left[ \mathbf{E} + \frac{1}{c} \mathbf{v} \times \mathbf{B} \right], \quad (4.1)$$

where  $\gamma$  is the Lorentz energy factor of a beam electron and  $m$  is the rest electron mass. In what follows, the fields are not self-consistent, in that the mutual effect of the beam particles upon one another is neglected. However, self-field effects

TABLE II. Simulation parameters of the MICA.

| Electron beam parameters            |                                       |
|-------------------------------------|---------------------------------------|
| Initial electron energy             | $\gamma_0 = 13$                       |
| Maximum initial transverse velocity | $\beta_{\perp} = 2.60 \times 10^{-3}$ |
| Initial axial velocity (6 MeV)      | $\beta_z = 0.9970$                    |
| Beam radius (cm)                    | $r_b = 0.05$                          |
|                                     | $r_b/R = 0.032$                       |
| Waveguide parameters                |                                       |
| Waveguide radius (cm)               | $R = 1.59$                            |
| Radius of vacuum hole (cm)          | $a = 0.48$                            |
|                                     | $a/R = 0.30$                          |
| Dielectric constant (alumina)       | $\epsilon = 9.4$                      |
| Waveguide length (cm)               | $z = 150$                             |
| Waveguide mode                      | $TM_{01}$                             |
| Radiofrequency wave                 |                                       |
| Field power (MW)                    | $P = 15$                              |
| Maximum field strength (MV/m)       | $E_{z\max} = 6.29$                    |
| Frequency (GHz)                     | $f_0 = 2.856$                         |
| Normalized phase velocity           | $V_{ph}/c = 0.9943$                   |
| Free space wavelength (cm)          | $\lambda_0 = 10.50$                   |
| Waveguide wavelength (cm)           | $\lambda_g = 10.46$                   |

have been taken into account in simulation studies using PARMELA as described below. As will be shown, self-fields are of minor consequence for the beam currents considered for the MICA. The three components of the force Eq. (4.1) in cylindrical form are

$$\dot{\beta}_r - \mu\beta_{\theta} = -\frac{e}{mc^2\gamma}[(1-\beta_r^2)E_r - \beta_r\beta_z E_z - \beta_z B_{\theta}], \quad (4.2)$$

$$\dot{\beta}_{\theta} + \mu\beta_r = -\frac{e}{mc^2\gamma}[-\beta_{\theta}\beta_r E_r - \beta_{\theta}\beta_z E_z], \quad (4.3)$$

and

$$\dot{\beta}_z = -\frac{e}{mc^2\gamma}[-\beta_z\beta_r E_r + (1-\beta_z^2)E_z - \beta_r B_{\theta}], \quad (4.4)$$

where  $\mu = \dot{\theta}$  is the normalized angular velocity of electron and the overdot represents the time derivative of the quantities  $d/d\tau$ ,  $\tau = ct$ .

The numerical simulation is based on the force Eqs. (4.2)–(4.4) with the field components given by Eqs. (2.6)–(2.11). The parameters used are listed in Table II. The input 6-MeV electrons from the rf gun are taken to be monoenergetic but with small transverse velocities that vary randomly from particle to particle. At the entrance of the waveguide they are randomly distributed inside the beam cross section as shown in Fig. 5(a1). Their distribution in  $\beta_x$ - $\beta_y$  space is shown in Fig. 5(b1).

The acceleration of electrons in the MICA is mainly axial because the intense axial field  $E_z$  dominates the other field components near the axis. In Fig. 6(a) we show the result for 15-MW traveling wave power. The electron energy increases almost linearly as the particles move down the waveguide. An analytical derivation from Eqs. (4.2)–(4.4) leads to

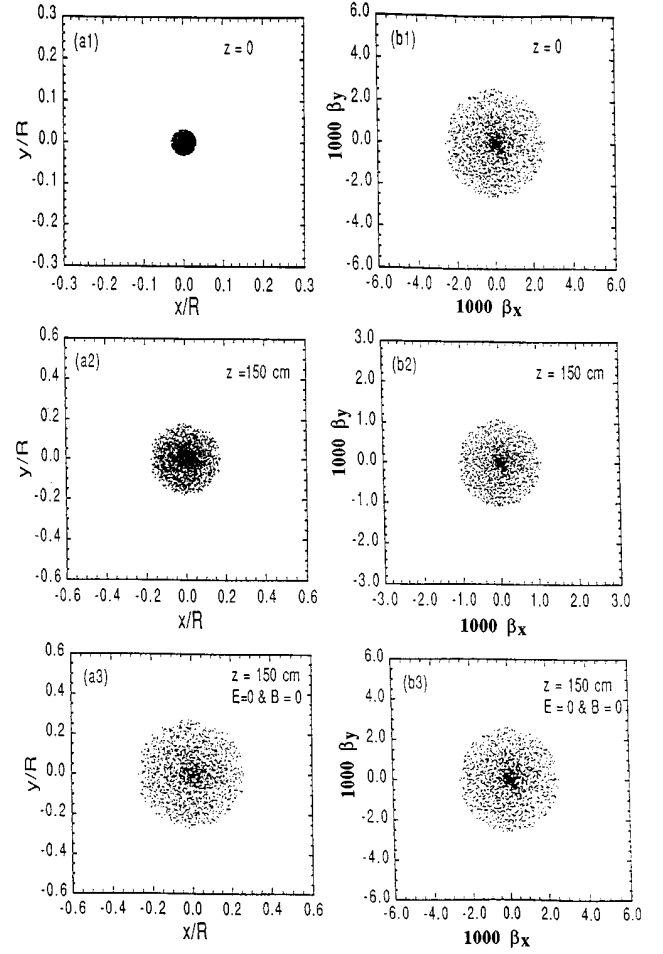


FIG. 5. Beam cross section in  $x$ - $y$  space and  $\beta_x$ - $\beta_y$  space (a1) and (b1) at the entrance of waveguide, (a2) and (b2) at the end of waveguide with the  $TM_{01}$  mode inside, and (a3) and (b3) at the end of waveguide with no rf fields. The vacuum hole radius  $a/R = 0.30$ .

$$\frac{d\gamma}{d\tau} = -\frac{e}{mc^2}[\beta_r E_r + \beta_z E_z], \quad (4.5)$$

which explicitly gives an approximate energy expression as

$$\gamma^2 = 1 + \left[ \sqrt{\gamma_0^2 - 1} - \frac{eE_0\tau}{mc^2} \right]^2, \quad (4.6)$$

where  $\gamma_0$  is the initial electron energy. When  $\gamma_0$  is large ( $\gamma_0 = 13$ , for example, in this case), the above equation can be further simplified as  $\gamma = \gamma_0 + e|E_0|\tau/mc^2$ . When  $|E_0| = 210$  statvolt/cm ( $= 63$  kV/cm),  $\tau = 150$  cm, it gives  $\gamma = 31.5$ , in close agreement with the simulation result. The validity of Eq. (4.6) requires that the relative phase of the electrons with respect to the rf field is equal to  $\pi$ ; checking the field distribution in Fig. 2, one sees that this corresponds to an initial distribution of particles at the position  $\lambda_g/2$ . Particles in this position will experience the maximum axial field, as we show in Fig. 6(b). Also shown in Fig. 6 (as dotted lines) is the result when 10% of power depletion is taken into account, which does not drop the particle energy too much. Due to the small difference between the electron

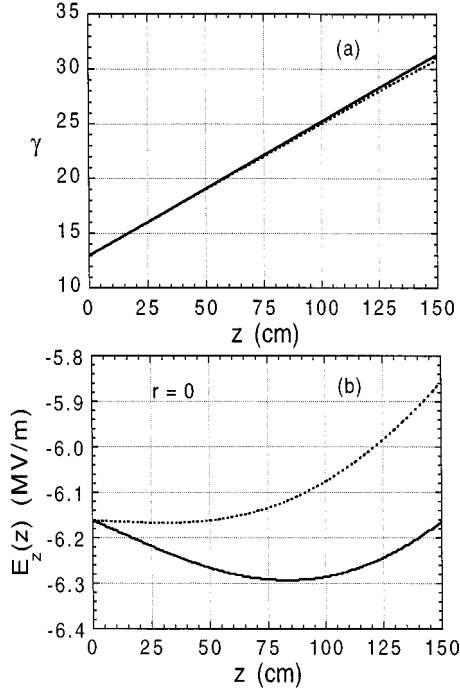


FIG. 6. (a) Electron energy as a function of the axial distance and (b) the axial accelerating field seen by one particle as it moves down the waveguide. The dotted lines are the case when a 10% power depletion is taken into account.

velocity and the wave phase velocity, one may expect that the electron will gradually slip from the maximum acceleration position, forward or backward depending on whether the beam is going faster or slower. In the current simulation, we find a phase slippage of  $\Delta\phi \approx 24^\circ$  in 1.5 m with the electrons moving ahead of the rf field, corresponding to a slippage interval of  $\Delta\tau_0 \approx 23$  ps. For a rf gun with a beam bunch length of only  $\Delta\tau_0 = 5$  ps, we can expect excellent trapping and acceleration of electrons during the entire propagation along the waveguide, without a taper of the dielectric element. In our calculation, the electron energy increases to about 16 MeV in 150 cm. If the dielectric surface breakdown strength is adequate, the electron energy can increase more.

When the electrons are located in a small “phase window” of acceleration, the radial component of the field  $E_r$  will prevent the electrons from spreading out even though the particles have an initial transverse velocity distribution. Shown in Figs. 5(a2) and 5(b2) are the cross sections of the electrons in the beam at the end of the MICA in  $x$ - $y$  and  $\beta_x$ - $\beta_y$  space separately. Electrons remain well confined inside the hole in the dielectric and the transverse velocity spread shrinks. An algebraic analysis from Eqs. (4.2)–(4.4) gives

$$\frac{1}{2} \frac{d\beta_\perp^2}{d\tau} = -\frac{e}{mc^2\gamma} [(1 - \beta_\perp^2)\beta_r E_r - \beta_\perp^2 \beta_z E_z - \beta_r \beta_z B_\theta], \quad (4.7)$$

where  $\beta_\perp^2 = \beta_r^2 + \beta_\theta^2$ . An approximate solution of Eq. (4.7) can be obtained when  $\beta_z \rightarrow 1$  and  $\beta_\theta^2 \ll \beta_r^2$ , namely,

$$\beta_\perp = \beta_{\perp 0} \exp \left[ \frac{eE_0\tau}{mc^2\gamma} \left( \frac{1}{2} \Delta k \tau \sin\phi_0 + \cos\phi_0 \right) \right], \quad (4.8)$$

where  $\phi_0$  is the initial phase of electrons,  $\Delta k = k_z - k_0 = 3.5 \times 10^{-3}$ , and when  $\phi_0 = \pi$ ,  $\bar{\gamma} = 22$ , we get  $\beta_\perp = 1.1 \times 10^{-3}$ , which is consistent with the maximum  $\beta_\perp$  in Fig. 5(b2). This calculation shows indeed that radial motions in the MICA are sufficiently constrained by the rf fields to maintain a small beam cross section and that particles are confined close to the axis so long as  $\phi_0 \sim \pi$  and  $\Delta\phi \ll 1$ . By contrast, shown in Figs. 5(a3) and 5(b3) is the beam cross section with no rf field in waveguide: in this case the beam cross section in  $\beta_x$ - $\beta_y$  space does not change, whereas in  $x$ - $y$  space is spreads uniformly. Beam spreading becomes serious when electrons are out of acceleration phase. For instance, when particles are initially injected somewhere near  $z_0 = 0, \lambda_g$  or  $\phi_0 = 0, 2\pi$ , our simulation found that the beam can neither be accelerated nor focused; instead the electrons will spread radially and collide with the dielectric wall.

In order to further examine radial stability of the MICA acceleration process, simulations for an injected off-axis beam have been carried out. For example, when the initial off-axis radial displacement was taken to be 0.5 mm, the off-axis displacement at the end of the waveguide remained at 0.5 mm and the beam cross section remains symmetrical. This is not too surprising since, by reference to the field distribution shown in Fig. 4, one observes that a small offset of the beam from the axis does not change by much the fields experienced by the beam. Furthermore, since  $E_{r1} \approx -E_0(k_z r) \sin\phi$  and  $\beta_{\theta 1} \approx -E_0(k_0 r) \sin\phi$ , the radial forces on an off-axis  $z$ -directed relativistic particle nearly cancel when the phase velocity of wave is close to the speed of light.

## V. SELF-FIELD EFFECT AND EMITTANCE EVOLUTION

Let us now include the self-field effect of electron current in beam dynamics. The space charge field of a bunch can be approximately determined by the formula for the terminal space charge field of a cylindrical beam [13]

$$E_s = \frac{0.18q}{a_0^2} \left[ 1 + \frac{a_0}{\gamma l} - \sqrt{1 + \left( \frac{a_0}{\gamma l} \right)^2} \right], \quad (5.1)$$

where  $E_s$  is the longitudinal space charge field in MV/m,  $a_0$  is the beam radius in cm,  $l$  is the bunch length in cm, and  $q$  is the total charge of the bunch in nC. For a bunch of peak current 10 A with bunch length  $\tau = 5$  psec one has  $q = 0.05$  nC,  $l = 0.15$  cm, and if the beam radius  $a_0 = 0.05$  cm, we have  $E_s = 0.094$  MV/m, a value that is far below the anticipated applied axial rf field of  $E_z = 6.3$  MV/m. Although this suggests that one can neglect the space charge for this level of  $q$ , we wish to determine if there are more subtle changes in the bunch quality; for this purpose we have conducted simulations of the MICA using the PARMELA accelerator code [14].

PARMELA is a versatile multiparticle electron linear accelerator code that is widely used in accelerator community [15]. In PARMELA, the electron beam, represented by a collection of macroparticles, may be transformed through a lin-

TABLE III. PARMELA results about beam emittance and energy spread at the entrance and exit of the waveguide.

| $z$<br>(cm) | $a_0$<br>(mm) | $E_{\text{beam}}$<br>(MeV) | $4\sigma_\phi$<br>(deg) | $4\sigma_E$<br>(keV) | $\varepsilon_{nx\text{rms}}$<br>( $\pi$ mm mrad) | $\varepsilon_{ny\text{rms}}$<br>( $\pi$ mm mrad) | $\varepsilon_{nz\text{rms}}$<br>( $\pi$ deg keV) |
|-------------|---------------|----------------------------|-------------------------|----------------------|--|--|--|
| 0           | 0.5           | 6.0                        | 5.78                    | 68.9                 | 3.05   | 2.90   | 24.9   |
| 150         | 3.0           | 15.6                       | 5.83                    | 80.2                 | 3.05   | 2.91   | 25.8   |

ear accelerator and/or transport system. The self-field effects (both electric and magnetic) are automatically taken into account in the simulation. Since the code usually applies to a periodic loading structure, it was necessary to modify the code so that it has the capability of modeling traveling-wave acceleration in the smooth-bore MICA structure, based on the field distribution given by Eqs. (2.6)–(2.11). In Table III we summarize some parameters of main interest for a bunch at the entrance ( $z=0$ ) and the exit ( $z=150$  cm) of the waveguide. Entrance conditions are taken from the rf gun and beam line computation, while the output is determined by our simulation results. The input parameters for the simulation are displayed in Fig. 7. The initial parameters in our PARMELA simulations are the same as we used in the single-particle dynamics run shown in Table II, except a bunch charge of  $q=0.05$  nC is now included.

Comparing the PARMELA output results (Fig. 8) with the single-particle results (Fig. 5), we find that in both simulations the acceleration gradients, the final particle energy, the beam cross section, and the particle velocity evolution are all in excellent agreement. The 1000 particles used in PARMELA simulation are all “good” particles, meaning that there is no particle loss in the MICA. PARMELA shows very clearly that

the transverse emittance  $\varepsilon_{nx\text{rms}}$  and  $\varepsilon_{ny\text{rms}}$  are constant throughout the acceleration, even though the longitudinal emittance  $\varepsilon_{nz\text{rms}}$  has a very slight change because of the minute longitudinal bunching that makes the particle energy spectrum more narrow. This PARMELA simulation is also compared to a test run where the net charge is set to zero: we observe only trivial differences. This shows that the self-field effects are not significant in any meaningful detail. However, when the beam current is increased, the self-field effects do affect the ultimate beam quality. For PARMELA runs with 20-A peak micropulse current a noticeable growth in normalized transverse and longitudinal emittance is found, while for 200 A the growth is substantial. These results suggest that achievement of the goal of a normalized transverse emittance of  $5\pi$  mm mrad for  $0.16\text{-nC}$  ( $10^9$ ) particles, 5-psec bunch is realistic.

## VI. MEASUREMENT OF THE DIELECTRIC BREAKDOWN LIMIT

### A. Analysis of loaded cavity resonator

The MICA, as described thus far, is a traveling-wave accelerator; however, an alternative arrangement would em-

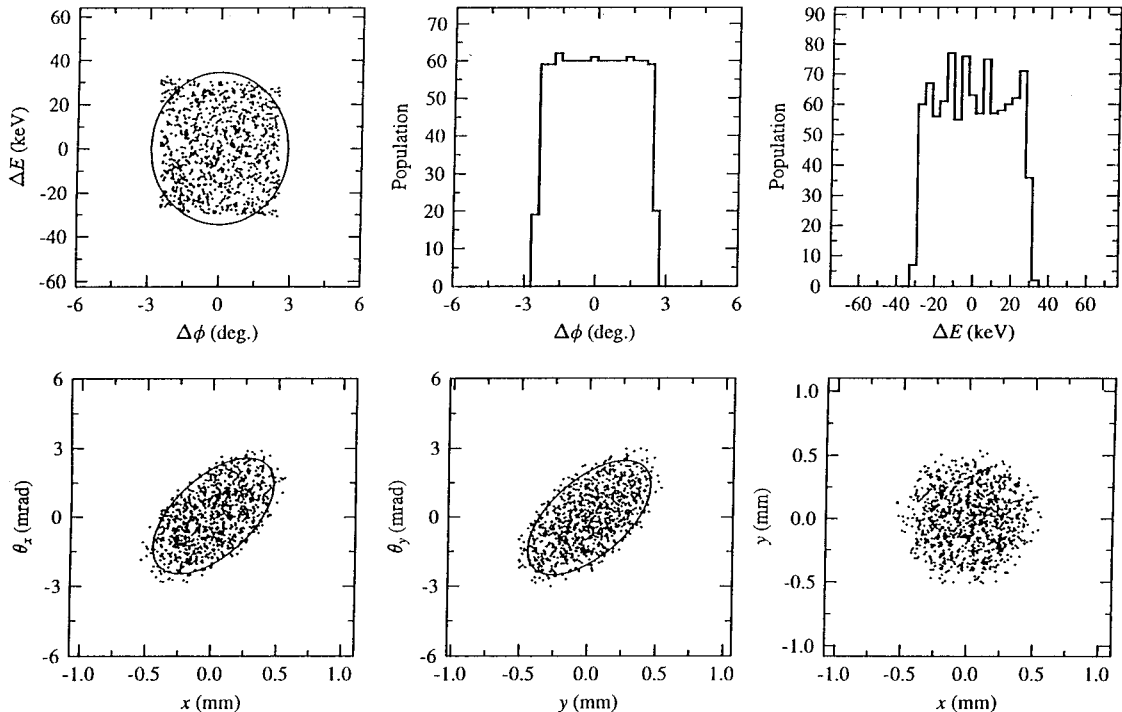


FIG. 7. Initial emittance, energy spectrum, and beam cross section of the electron bunch when the space charge effect is taken into account,  $q=0.05$  nC.

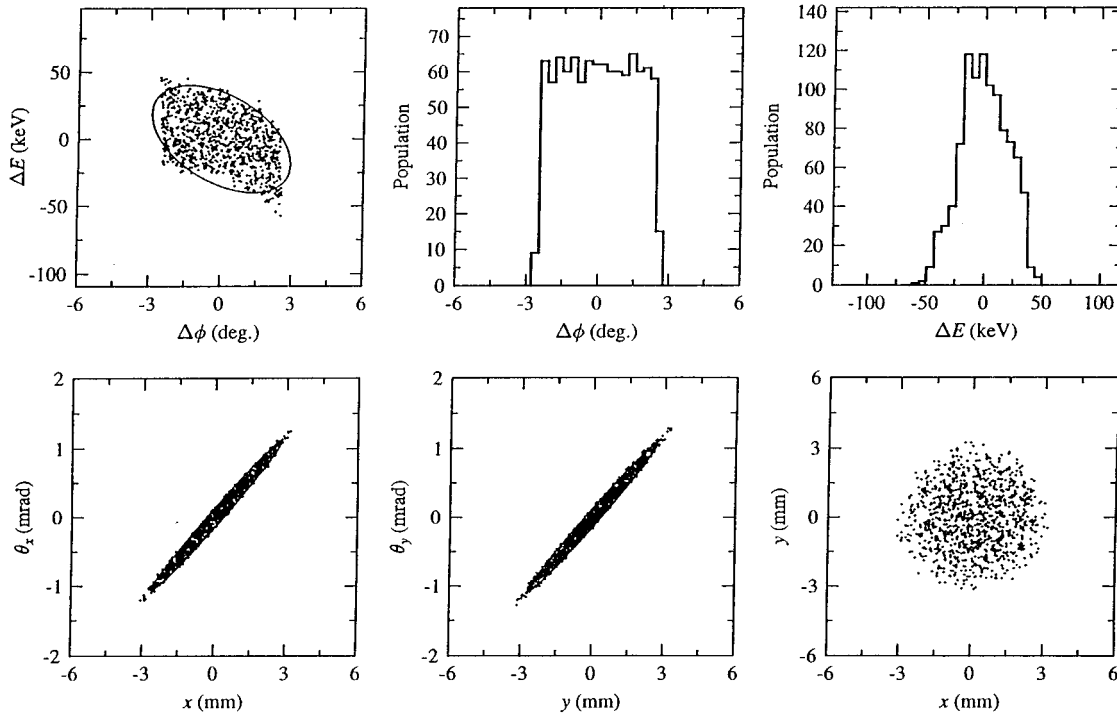


FIG. 8. Beam distribution at the exit of the lined waveguide. The transverse normalized emittance is constant, the longitudinal emittance has a very slight change, the energy spread becomes narrower, and the cross section of the bunch expands as if there is no space charge effect.

ploy a reflector at one end to allow standing waves to build up, so that a higher accelerating gradient could be obtained for a given rf power. Also, in order to determine the breakdown limits at 2.856 GHz, we have designed and constructed a cavity resonator with an alumina liner. Thus it is worthwhile to derive formulas for the resonance frequency and quality factor  $Q$  for a TM resonator constructed with a section of dielectric-lined waveguide with conducting plates closing the ends. Since the exact value of the alumina dielectric constant of the sample we used was not accurately known, we began with a low-power test of the resonant modes of a simple cavity incorporating an alumina annulus with metallic surfaces, which is coupled to a signal generator and a detector as shown in Fig. 9.

For a cylindrical cavity of axial length  $d$ , the rf fields are a superposition of forward and backward traveling waves of

the forms given by Eqs. (2.6)–(2.11). For the component  $E_z$ , superposition of equal amplitude waves gives, in regions 1 (hole) and 2 (dielectric), the form

$$E_{z1}(r, z, t) = E_{c0} I_0(k_{1r} r) \cos(k_{zp} z) \cos(\omega t) \quad (0 \leq r \leq a) \quad (6.1)$$

and

$$E_{z2}(r, z, t) = E_{c0} G_0(k_{2r} r) \cos(k_{zp} z) \cos(\omega t) \quad (a < r \leq R), \quad (6.2)$$

where  $E_{c0}$  is the amplitude of the standing wave, and to satisfy the boundary conditions of zero tangential electric field at the end planes, the axial wave number takes on discrete values  $k_{zp} = p\pi/d$ ,  $p=0, 1, 2, \dots$ . Correspondingly, the cavity resonance frequency is

$$\omega_{0np} = \frac{c}{\sqrt{\epsilon_1}} \left[ -k_{1in}^2 + \left( \frac{p\pi}{d} \right)^2 \right]^{1/2} = \frac{c}{\sqrt{\epsilon_2}} \left[ k_{2n}^2 + \left( \frac{p\pi}{d} \right)^2 \right]^{1/2}. \quad (6.3)$$

For a given microwave frequency  $\omega$  (e.g.,  $\omega = 2\pi \times 2.856$  GHz) and resonance mode  $TM_{0np}$  and using the eigenvalue of the lined waveguide we solved in Sec. II, Eq. (6.3) will give the longitudinal dimension  $d$ . Conversely, if the resonance frequency is measured for resonator of given length, Eq. (6.3) can be used to find the value of the dielectric permittivity  $\epsilon_2$ .

The unloaded quality factor  $Q$  of the cavity can be expressed as

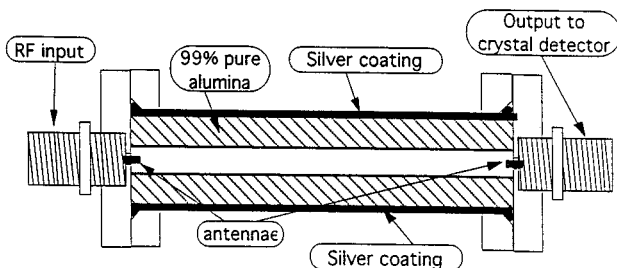


FIG. 9. Sketch of the test resonator fabricated from a short section of alumina pipe coated on its exterior with silver paint. A low power rf input was used.

$$\frac{1}{Q} = \frac{1}{Q_w} + \frac{1}{Q_d}, \quad (6.4)$$

with contributions from wall losses and dielectric losses expressed as  $Q_w = \omega(U_s/P_w)$  and  $Q_d = \omega(U_s/P_d)$ , where  $U_s$  is the time-average energy stored in the cavity,  $P_w$  is the Ohmic losses on the wall, and  $P_d$  is the dielectric losses. To determine the  $Q$  of a cavity, we need to calculate the time-average energy stored in the cavity and then determine the power loss in the walls and in the dielectric. The integral of (3.6) over the cavity length yields the energy stored in the cavity

$$\begin{aligned} U_s = \int_0^d U dz = & \frac{k_0^2}{8\pi} \left\{ \frac{\epsilon_1^2}{k_{\perp 1}^2} \int_0^d dz \int_{A_1} |E_{z1}|^2 dA \right. \\ & + \frac{\epsilon_2^2}{k_{\perp 2}^2} \int_0^d dz \int_{A_2} |E_{z2}|^2 dA \\ & \left. + 2\pi a \int_0^d \left[ E_{z1}^* \frac{\partial E_{z1}}{\partial r} \right]_{r=a} dz \frac{\epsilon_1}{k_{\perp 1}^2} \left[ \frac{\epsilon_1}{k_{\perp 1}^2} - \frac{\epsilon_2}{k_{\perp 2}^2} \right] \right\}. \end{aligned} \quad (6.5)$$

Considering the Ohmic losses on both the sidewall and the two ends of the cavity, the power loss at the walls is

$$\begin{aligned} P_w = \frac{c^2}{32\pi^2 \sigma \delta} \left\{ \frac{\epsilon_2^2 k_0^2}{k_{\perp 2}^4} \int_0^d dz \oint_C \left| \frac{\partial E_{z2}}{\partial n} \right|_{r=R} dl \right. \\ \left. + 2 \frac{\epsilon_1^2 k_0^2}{k_{\perp 1}^4} \int_{A_1} |\nabla_{\perp} E_{z1}|_{z=0}^2 dA + 2 \frac{\epsilon_2^2 k_0^2}{k_{\perp 2}^4} \int_{A_2} |\nabla_{\perp} E_{z2}|_{z=0}^2 dA \right\}. \end{aligned} \quad (6.6)$$

The dielectric losses can be determined from the electrical conductivity  $\sigma_d = (\omega/4\pi)\epsilon_i$ , leading to the result

$$P_d = \frac{1}{2} \frac{\omega}{4\pi} \epsilon_i \int_0^d dz \int_{A_2} \left[ \frac{k_z^2}{k_{\perp 2}^4} \left| \frac{\partial E_{z2}}{\partial r} \right|^2 + |E_{z2}|^2 \right] dA. \quad (6.7)$$

The design parameters of an ideal cavity resonator, based on the sample available, are listed in Table IV. The cavity operates in the  $TM_{012}$  mode; that is, the length of the cavity is one guide wavelength of the  $TM_{01}$  waveguide mode. The cavity has a moderate quality factor  $Q=4620$ . The relation between the maximum axial field in the cavity and the power coupled in is also given in Table IV in terms of the parameter  $E_{z\max}/P^{1/2}$ , where  $P$  is the total power lost in both walls and dielectric.

### B. Measurements of a loaded cavity resonator and breakdown results

Measurements were conducted with a resonator fabricated from a short section of alumina pipe coated on its exterior with silver (Fig. 9). The alumina samples, supplied by LSP Ceramics, Inc., had inner and outer radii of 1.429 and 0.508 cm, respectively. There are some differences in dimensions between the proposed waveguide and the test cavity (the outer radius is 10% smaller than the required value of 1.5875

TABLE IV. Simulation parameters of dielectric-loaded cavity resonator.

| Cavity parameters   |  |
|---|--|
| Radius of empty hole (cm)                                     | $a=0.508$                                  |
| Radius of cylindrical cavity (cm)                             | $R=1.429$                                  |
|   | $a/R=0.356$                                |
| Length of cavity (cm)   | $d=12.11$                                  |
| Real part of the dielectric constant                          | $\epsilon_r=9.62$                          |
| Imaginary part of the dielectric constant                     | $\epsilon_i/\epsilon_r=9.4 \times 10^{-5}$ |
| rf wave parameters  |  |
| Cutoff frequency (GHz)  | $f_c=3.118$                                |
| Resonance frequency (GHz)                                     | $f_0=3.210$                                |
| Transverse wave number in the hole ( $\text{cm}^{-1}$ )       | $k_{1r}=0.4281$                            |
| Transverse wave number in the dielectric ( $\text{cm}^{-1}$ ) | $k_2=2.021$                                |
| Wavelength in the cavity resonator (cm)                       | $\lambda_g=12.11$                          |
| Cavity mode   | $TM_{012}$                                 |
| Quality factor of the cavity                                  |  |
| $Q$ for the conducting walls                                  | $Q_w=7929$                                 |
| $Q$ for the dielectric  | $Q_d=11070$                                |
| $Q$ of the cavity   | $Q=4620$                                   |
| Power loss ratio (MV/m)/(MW) <sup>1/2</sup>                   | $E_{\max}/P^{1/2}=20.32$                   |

cm, while the inner radius is 7% larger). Nevertheless, measurements on the samples available still provide a good test of theory. Raw data for the observed rf transmission by the cavity is shown in Fig. 10(a), over a frequency range between 3 and 6 GHz. Figure 10(b) shows a plot of the square of the 12 observed resonance frequencies in Fig. 10(a) versus the square of the resonance index. From Eq. (6.3), one sees that the slope of this line should be the reciprocal of the relative dielectric constant; for the data in Fig. 10(b), this reciprocal slope is 9.62. This differs from 9.4, the canonical value taken in the analysis given above, but 9.62 is well within the range quoted for good purity alumina. It is highly significant that no other resonances for this structure between 3 and 6 GHz were found that did not fit on the line shown in Fig. 10(b), despite attempts having been made to excite non-axisymmetric modes using a nonaxisymmetric antenna. One can conclude from this observation that potentially disruptive nonaxisymmetric modes of the dielectric pipe were not excited. Calculation of the properties of non-axisymmetric modes would be a formidable task, one that these experimental tests appear to render unnecessary.

The vertical intercept for the line in Fig. 10(b) should be the square of the  $TM_{01}$ -mode waveguide cutoff frequency, which in this case is observed to be 3.216 GHz. For  $\epsilon_2=9.62$ ,  $R=1.429$  cm, and  $a=0.508$  cm, the calculated value is 3.118 GHz, a value of 3.05% lower than the measurement. This discrepancy is not unreasonable, considering the added circuit reactance of the coupling antennas and the incomplete closure of the end walls. Typical  $Q$  values for the observed cavity resonances were in the range of 400–500, much lower than the calculated unloaded value of 4620. This is also not too surprising, considering the open ends of the beam hole and the strong external loading that was required to make accurate resonance measurements on all 12 modes. However, this exercise emphasizes the need to carefully test alumina samples prior to acceptance and prior to selection of

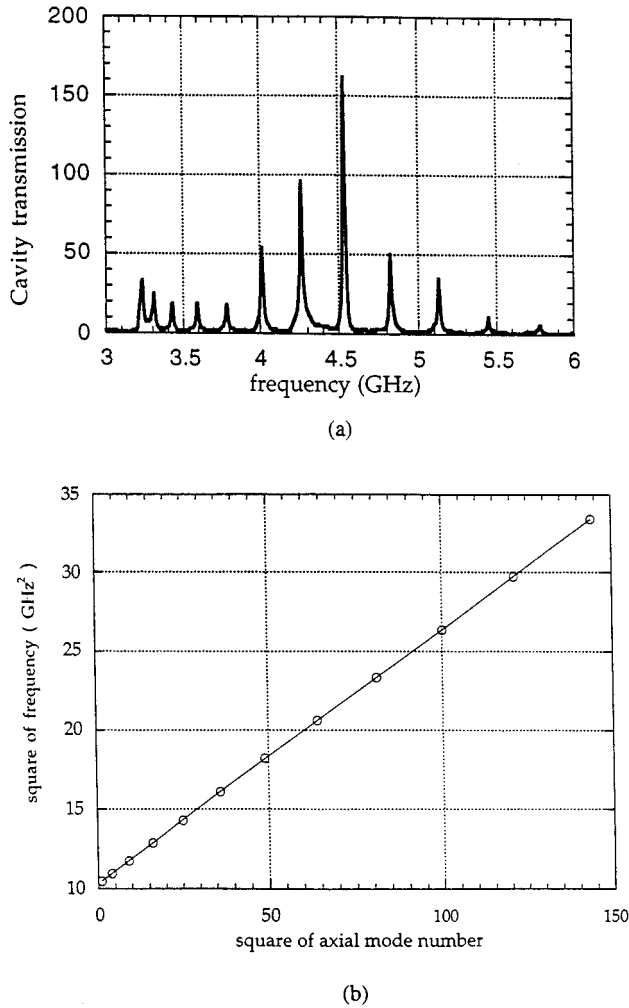


FIG. 10. (a) Mode spectrum of the resonator obtained in measurement-cavity transmission in arbitrary units and (b) square of the mode resonance frequency versus the square of the axial mode number from measurements on the resonator shown in (a). The reciprocal of the slope of the line is 9.62, which can be inferred to be the dielectric permittivity  $\epsilon_2$ , from Eq. (6.3).

the final parameters for the 150-cm accelerating sections. In particular, an accurate advance measurement of dielectric constant, phase velocity, and loss tangent must be made from samples taken from the alumina batch to be used for the final accelerating sections.

Measurements using high-power microwaves applied to the alumina samples were also carried out to determine rf breakdown limits. Since the cavity described above has resonances above 3.2 GHz, an alternative experimental arrangement was devised to subject the alumina surfaces to high tangential rf electric fields at 2.856 GHz (obtained from a SLAC klystron). A diagram of the arrangement used is shown in Fig. 11. A standing-wave resonance was established in WR-284 rectangular waveguide using inductive irises. Measurements with the alumina sample in place showed this arrangement to give an effective gain of over 11 dB, as deduced from signals on the sample probe with and without the irises. Under these conditions, the peak tangential rf electric field at the inner alumina surface is calculated

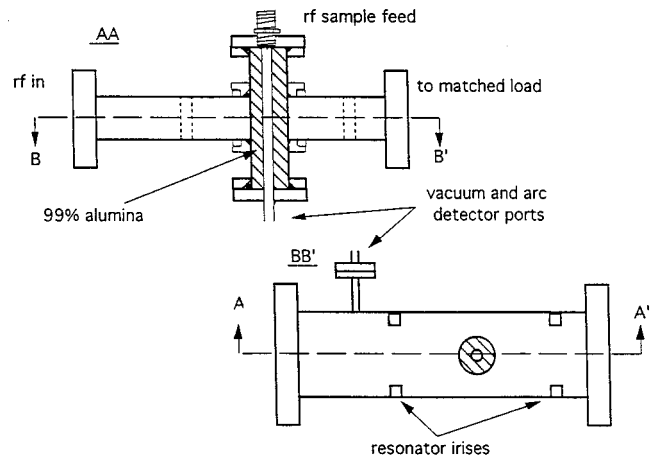


FIG. 11. Sketch of the experimental arrangement used to measure the maximum tangential rf electric field that can be sustained at an alumina surface.

to be  $33.6P^{1/2}$  V/cm, where  $P$  is the incident power in watts. This indicates that a field of 63 kV/cm would be applied when  $P=3.52$  MW. In the experiments, the rf power level was increased over an  $\sim 12$ -h period to provide gradual rf processing of the structure, without allowing the background pressure to exceed  $2 \times 10^{-6}$  Torr. It was found that this procedure could be continued up to a power level of 6.25 MW, without evidence of arcing at the alumina surface. This corresponds to a tangential field of 84 kV/cm. These observations suggest that acceleration gradients of at least 8.4 MV/m should be achievable in the MICA, where a design with superior vacuum integrity and coating of the alumina is planned.

## VII. CONCLUSIONS

We have studied a microwave inverse Čerenkov accelerator, which has an acceleration mechanism similar to that of a conventional rf linear accelerator. However, the accelerating structure, which comprises a continuous coated ceramic pipe, should be less expensive to fabricate than that of the linear accelerator. In the absence of any periodic loading structures in the waveguide, wake-field generation that can lead to emittance growth and beam breakup should be minimized. Thus MICA's advantages of a relatively compact structure, smooth-bore design, and no need of magnetic focusing make it a very competitive facility as a simple, low-cost electron accelerator.

In this paper, we have studied numerically the eigenmode, field profile, energy flow, particle dynamics, and space charge effects; experimentally, we measured the dielectric breakdown limit of alumina. We find that a thick liner with a high dielectric constant is very helpful not only to store high rf energy but also to maintain an intense and uniform axial accelerating field in the central hole. The particle motion in the waveguide is nearly one dimensional with all input particles being accelerated and no interception by the dielectric. There is no beam breakup and the beam bunches have good stability even if they are slightly off axis. For the beam current under consideration, the space charge effect is not an issue and the initial low normalized emittance, within  $3\pi$

mm mrad, is constant throughout the acceleration. The acceleration gradient in the simulation is 6.3 MeV/m, in which case the electron energy increases from 6 to 16 MeV in 150 cm. However, without exceeding the breakdown limit measured by experiment (greater than 8.4 MeV/m) and using higher microwave power and/or a higher- $Q$  structure, the electron energy could increase even more, perhaps in the range of 10–15 MeV/m if techniques for improving the dielectric breakdown [9] on the surface using Ti or TiN evaporated coatings can be used successfully.

We identify some challenging technical issues such as the finish machining of the waveguide and liner, since the phase velocity of a rf wave in the vicinity of the speed of light is

very sensitive to the radius of the vacuum hole and tube. Also, one must pay attention to the matching of the power feeding system and the accelerator waveguide because of the substantial difference of the wave group velocity (or impedance) in these two sections.

#### ACKNOWLEDGMENTS

This work is sponsored by the DOE, Division of High Energy Physics. The authors acknowledge Dr. Hongxiu Liu of CEBAF for his assistance in running PARMELA for space charge effect simulation.

- 
- [1] J. E. Walsh, T. C. Marshall, and S. P. Schlesinger, *Phys. Fluids* **20**, 709 (1977).
  - [2] J. E. Walsh and E. Fisch, *Nucl. Instrum. Methods A* **318**, 772 (1992).
  - [3] W. Main, R. Cherry, and E. Garate, *Appl. Phys. Lett.* **55**, 1498 (1989).
  - [4] T. B. Zhang and T. C. Marshall, Proceedings of the 17th International Free Electron Laser Conference, New York, 1995 [*Nucl. Instrum. Methods Phys. Res. Sect. A* (to be published)].
  - [5] J. A. Edighoffer *et al.*, *Phys. Rev. A* **23**, 1848 (1981).
  - [6] J. R. Fontana and R.H. Pantell, *J. Appl. Phys.* **54**, 4285 (1983).
  - [7] R. D. Romea and W. D. Kimura, *Phys. Rev. D* **42**, 1807 (1990).
  - [8] W. D. Kimura *et al.*, *Phys. Rev. Lett.* **74**, 546 (1995).
  - [9] Y. Saito (unpublished).
  - [10] M. Shoucri, *Phys. Fluids* **26**, 2271 (1983).
  - [11] T. Moreno, *Microwave Transmission Design Data* (Dover, New York, 1958), Chap. 11.
  - [12] J. D. Jackson, *Classical Electrodynamics* (Wiley, New York, 1975), Chap. 8.
  - [13] H. Liu *et al.*, *Nucl. Instrum. Methods Phys. Res. Sect. A* **358**, 475 (1995).
  - [14] H. Liu (private communication).
  - [15] K. R. Crandall and L. Young, Los Alamos National Laboratory Report No. La-UR-90-1766, 1990 (unpublished), p. 137.